

BEARING METRICS FOR HEALTH MONITORING OF MACHINE TOOL LINEAR AXES

Gregory W. Vogl¹
 National Institute of Standards
 and Technology
 Gaithersburg, MD, USA

Brian C. Galfond
 Catholic University of America
 Washington, DC, USA

N. Jordan Jameson
 National Institute of Standards
 and Technology
 Gaithersburg, MD, USA

ABSTRACT

Diagnostics and prognostics of rotating machinery ball bearings is quite mature with an abundance of available methods and algorithms. However, extending these algorithms to other ball bearing applications is challenging and may not yield usable results. This work used a linear axis to study the ability of an inertial measurement unit (IMU), along with nine signal features, to measure changes in geometric error motions due to induced faults on the recirculating ball bearings of two carriage trucks. The IMU data was analyzed with the nine features used for rotating machinery systems, including root-mean-square, standard deviation, and kurtosis. For each stage of degradation, the statistical population and median value of each feature were compared against the population and median for no degradation, to monitor feature changes due to ball damage. Correlation analyses revealed an ability of the standard deviation feature to detect statistically significant changes as small as 0.05 micrometers or 0.5 microradians, corresponding to a total damaged surface area of truck balls of less than 0.1 percent.

Keywords: machine tool, smart manufacturing, linear axis, ball bearing, wear, degradation, diagnostics

1. INTRODUCTION

Linear axes are vital components in manufacturing, existing within machine tools to move cutting tools and workpieces to their desired positions for part production [1]. Figure 1A shows a typical linear axis, composed of four trucks (also called “linear motion guides”) that constrain a carriage to move along two rails (or “guideways”). As shown in Figure 1B, in addition to the commanded motion along the X-direction, the actual motion has three translational errors and three angular errors: one positioning error motion (E_{XX}), two straightness error motions (E_{YX} and E_{ZX}), and three angular error motions (E_{AX} , E_{BX} , and

E_{CX}). Typically, a machine tool includes multiple axes that degrade with use, leading to changes in geometric motion errors that affect the quality of the machined parts.

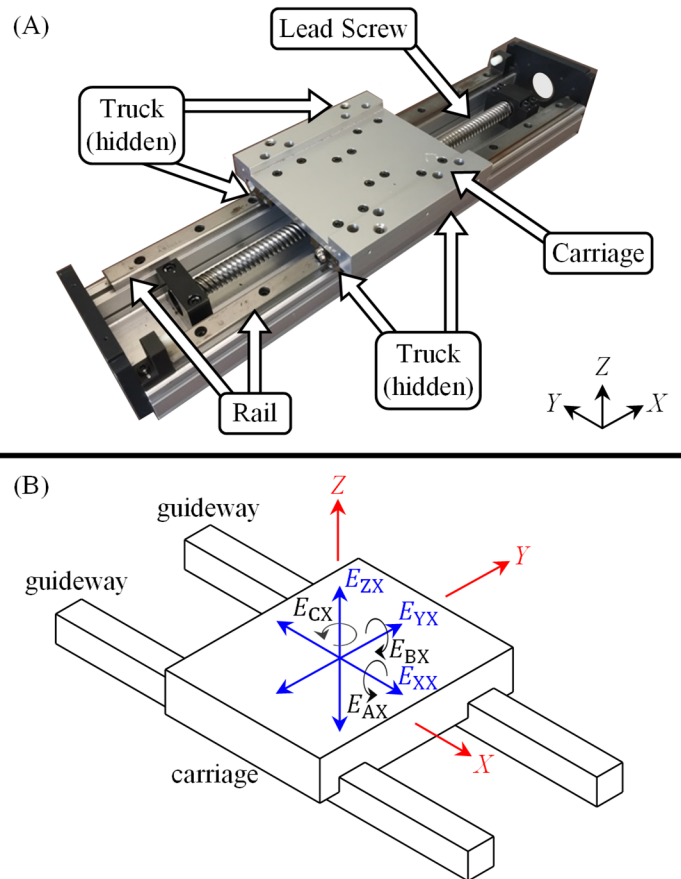


FIGURE 1: (A) LINEAR AXIS AND (B) GEOMETRIC ERROR MOTIONS.

¹ Contact author: gvogl@nist.gov

Ideally, once a linear axis is operational on a machine tool, all error motions are zero; but in practice, nonzero errors exist that contribute to the errors on the workpiece. These error motions tend to worsen with machine usage, aging, and crashes, since abrasion and adhesion between parts in linear axes causes material fatigue, pitting, cracking, and wear. This damage can result in faults developing in linear axis components, such as the rails, rolling element bearings, and/or ball screw [2, 3]. If not properly mitigated, these faults will grow to affect the quality of parts produced, leading to parts becoming out of tolerance and/or machine failure [4]. As demands for versatility and batch volume increase for manufacturing processes, machines are experiencing higher production loads, and as a result, the potential for faults and failures is becoming more common. Hence, machine tool monitoring and maintenance rules are needed to mitigate this accumulation of degradation and minimize the costs imposed by imperfect production and scrapped parts.

Mature methods exist for the fault detection and diagnostics of error motions, but they are manual, time consuming, and often cost prohibitive. The state-of-the-art instruments for linear axis error measurement (the basis for diagnostics) are explained in the International Organization for Standardization (ISO) 230-1 [5]: straightedge and linear displacement sensor, microscope and taut wire, alignment telescope, alignment laser, and laser straightness interferometer. These time-consuming measurements require a shutdown of the machine with a typical setup change and thus cannot provide in-situ diagnostics [6].

To enable proactive (not reactive) maintenance, manufacturers need automated methods for diagnosing machine tool linear axes without halting production. In 2010, Teti *et al.* [7] identified that intelligent sensor-based systems and advanced signal data processing need to be further developed to help decrease machine downtime and increase productivity, product quality, and knowledge of manufacturing processes. One possible advance lies in the use of an inertial measurement unit (IMU) consisting of a three degree-of-freedom (DOF) accelerometer and a three DOF rate gyroscope [8-10], as shown in Figure 2. Data from the IMU can be used to detect changes in the positioning, straightness, and angular error motions. IMU measurements can be made quickly and with little intrusion into the operation of the machine, resulting in data that provides insight into the condition of the linear axis. It has been shown to be effective at detecting rail degradation to similar levels of accuracy delivered by a laser interferometer [8].

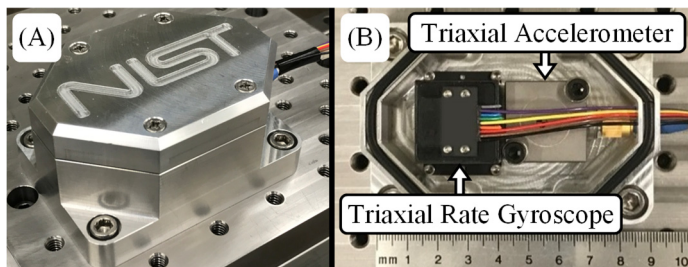


FIGURE 2: (A) ISOMETRIC VIEW OF IMU AND (B) TOP VIEW OF IMU WITHOUT ITS COVER.

However, a challenge remains in verifying the IMU’s capabilities for detecting degradation in the truck bearings of a linear axis. One complication is the multitude of rolling element bearings (typically hundreds of balls) within the bearing system, which causes a low signal-to-noise ratio (that can be less than 1) in the health monitoring data. The convolution of numerous ball imperfections affects the geometric error motions of the carriage, making it difficult to isolate small influences due to damage on a single ball. Accordingly, an experiment was designed to examine the sensitivity of the IMU-based error motions to artificially-induced damage on the truck bearings.

2. EXPERIMENTAL SETUP

Figure 3 shows the linear axis testbed used for data collection in this study. A lead screw rotates via a DC motor to move a carriage nominally parallel with the X-axis (Figure 3A). Four trucks with ball bearings contact two rails, to constrain the carriage to move in a nominally linear fashion. Each truck has two loops of balls (Figure 3B), an inner loop and outer loop, with each loop containing 32 balls. Correspondingly, each rail has an inner raceway and an outer raceway (Figure 3C). The two loops interact with different raceways (or grooves) in the rails, one inner and one outer. Whenever the carriage moves back and forth, the balls within the inner/outer loop of a truck rotate in and out of contact with the inner/outer raceway of the rail. At any given instant, about 13 balls per loop contact the given raceway of the rail. Hence, there are about 104 balls (13 balls per loop × 2 loops per truck × 4 trucks) in contact with the two rails.

Each truck was modified to be a “smart truck” equipped with an inductive proximity sensor to detect the phase of the outer loop of balls. Figure 4A shows how each truck (Truck 2 in the figure) was modified with a slot and a tapped access hole, in which resides an inductive proximity sensor. The sensor is used to detect the presence of a metallic or non-metallic ball in its proximity. Instead of using thirty-two chrome steel balls that come with each truck, six of the thirty-two balls were replaced with nylon balls. Figure 4B shows the pattern of twenty-six metal balls with six nylon balls utilized for the outer loop of each truck. Each ball in the pattern, whether metallic or non-metallic, has its own identification number. The pattern was chosen out of many possibilities so that, at any time, visual inspection of the balls through the slot yields a unique pattern of plastic and metal balls for identification. For example, based on Figure 4B, the visible pattern in Figure 4A begins on the left side of the slot with the fourth ball (a nylon ball).

During linear axis motion, the voltage output of the inductive proximity sensor switches with a frequency of 5 kHz between about 0 V (for the presence of nylon) to a nominal voltage when enough metal appears in front of the sensor. A cross-sectional schematic illustration (Figure 4C) reveals that a ball moves to within less than 0.8 mm of the front surface of the inductive proximity sensor, which is sufficient for detectability. By measuring the output voltage as the carriage moves, the phase of the outer loop of balls can be deduced based on the fact that

the zero-volt portions of the signal follow a known pattern (Figure 4B).

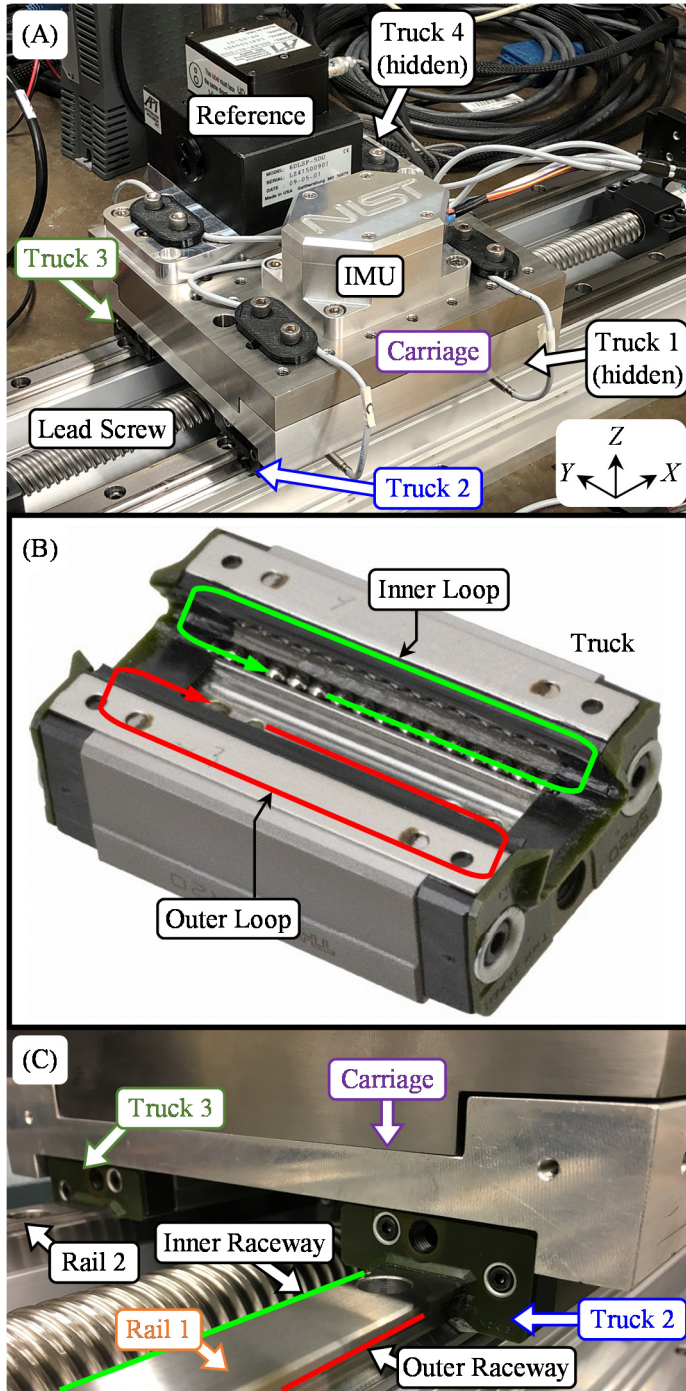


FIGURE 3: (A) LINEAR AXIS WITH IMU, (B) VIEW OF A TRUCK BOTTOM WITH LOOPS OF BALL BEARINGS EXPOSED, WHERE “INNER LOOP” CONTACTS INNER RACEWAY AND “OUTER LOOP” CONTACTS OUTER RACEWAY, AND (C) VIEW OF EXPERIMENTAL SETUP SHOWING TRUCK 2 ATTACHING TO RAIL 1 VIA RACEWAYS.

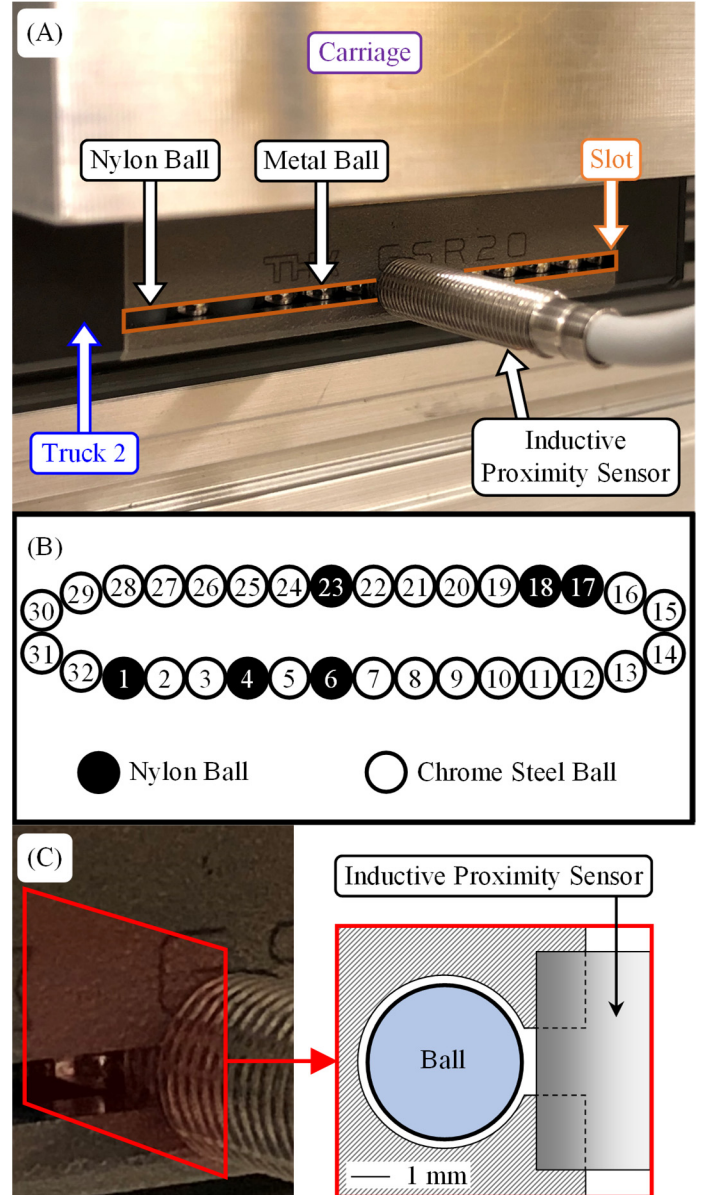


FIGURE 4: (A) VIEW OF A TRUCK WITH EMBEDDED INDUCTIVE PROXIMITY SENSOR, (B) PATTERN OF METALLIC AND NON-METALLIC BALLS USED IN OUTER BALL LOOP OF EACH TRUCK, AND (C) CROSS-SECTIONAL SCHEMATIC ILLUSTRATION OF A TRUCK WITH SENSOR.

3. EXPERIMENTAL PROCEDURE

In this experiment, the metal balls were progressively removed and degraded from the two trucks (Truck 1 and Truck 2) on Rail 1. Figure 5 shows the procedure for damaging a ball one at a time. First, a single ball is removed from the outer loop of a truck (Figure 5A). The tapped hole in the truck allows removal of a ball while leaving the carriage/truck/rail/lead screw system effectively unchanged. This was necessary because if the trucks were removed and then reassembled at each stage of degradation, then the load on each truck would change from one assembly to the next, which would change the error motions as

well. Hence, to eliminate the need for disassembly and reassembly of the trucks during the experiment and thus ensure that changes in error motions are due only to damage in outer loop balls, the trucks were modified with a tapped access hole (Figure 4A). Second, the ball is abrasively modified to have a flat with a nominal depth of $30\ \mu\text{m}$ (Figure 5B). Third, as seen in Figure 5C, the nominal diameter and the flat-to-sphere distance of the ball are measured with a micrometer and the difference of the two measurements is an estimate of the flat depth. Specifically, five measurements are performed for both the nominal diameter and the flat-to-sphere distance, and the difference of the respective averages is the estimated flat depth. Finally, the ball is placed back into its position in the outer loop of the truck.

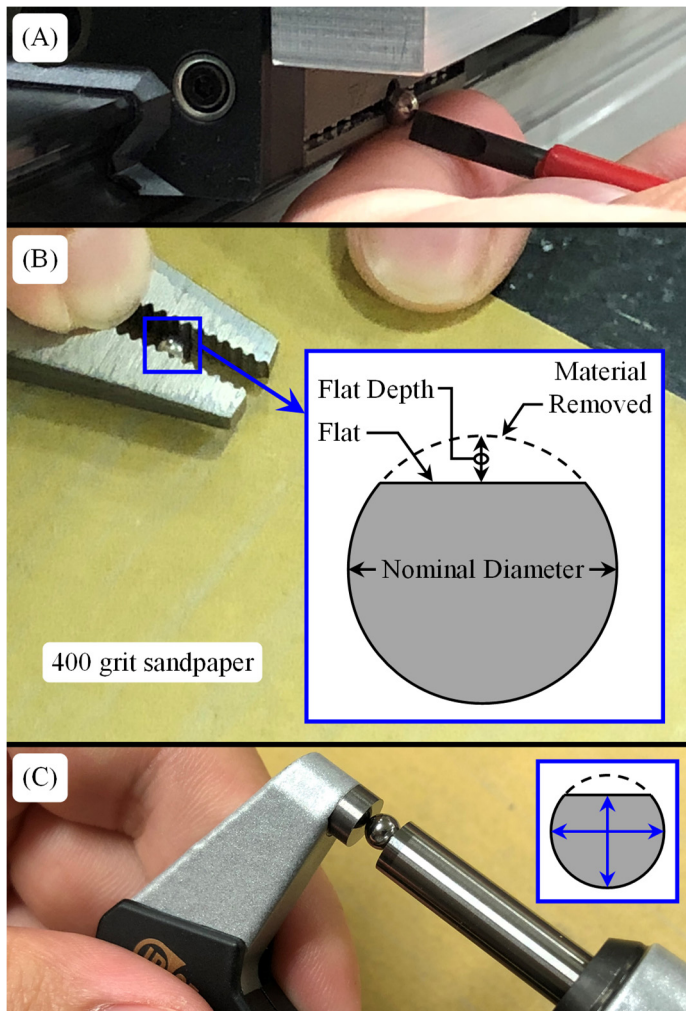


FIGURE 5: PROCEDURE FOR DAMAGING A BALL: (A) REMOVAL OF BALL FROM OUTER LOOP, (B) ABRASIVE REMOVAL OF MATERIAL TO CREATE FLAT, AND (C) ESTIMATION OF FLAT DEPTH WITH HANDHELD MICROMETER MEASUREMENTS.

Over the course of the experiment, each of the metal balls in the outer loop of Truck 2 was damaged in a specific order until

each ball had six flats, and then the same process was repeated for Truck 1. Figure 6 shows the order in which the twenty-six balls in the outer loop of a truck were damaged before a “damage cycle” is complete. The seemingly haphazard order was chosen *a priori* as an attempt to simulate random ball damage. Once four balls were damaged and placed back into Truck 2, fifty (50) runs of IMU data were collected. Each run consists of moving the carriage, forward and backward, at three different speeds: 0.02 m/s, 0.1 m/s, and 0.5 m/s. Also, ten (10) bidirectional runs of laser-based reference data were collected statically at 1 mm intervals. Then, another four balls were damaged, and data was collected again for that new “stage” of degradation. Table 1 shows the numbers of the outer loop balls in Truck 2 that were damaged at each of the thirty-nine stages of degradation, based on the damage cycle of Figure 6. Truck 2 was “fully damaged” once six damage cycles were completed; that is, each chrome-steel ball in the outer loop of Truck 2 had six flats (Stage 39 in Table 1). Finally, the same ball-damage process was repeated for Truck 1 (Stage 40 to Stage 55), except that only about 3 flats were induced on each ball in Truck 1. A total of 220 flats were induced on 52 balls (26 balls per truck) in the entire experiment. IMU and laser-based reference data were gathered at each stage of degradation (Stage 0 to Stage 55).

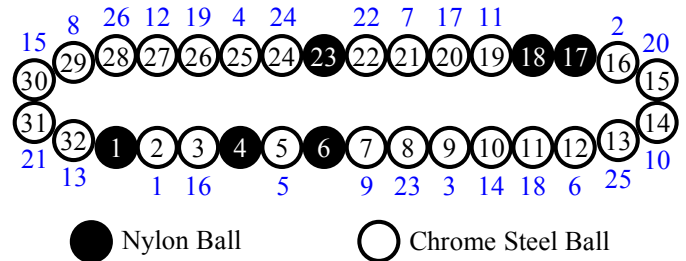


FIGURE 6: ORDER OF OUTER LOOP BALL DAMAGE. THE BLUE NUMBERS REPRESENT THE ORDER IN WHICH THE METAL BALLS ARE DAMAGED. WHENEVER A CYCLE IS COMPLETE (ALL TWENTY-SIX METAL BALLS HAVE SAME NUMBER OF FLATS), A NEW CYCLE MAY BEGIN.

Figure 7 shows histograms of the flat depths for all 220 flats induced on the metal balls in Truck 2 and Truck 1. Except for one outlier (not shown in Figure 7A), the flat depth ranges between $25\ \mu\text{m}$ and $35\ \mu\text{m}$ with an average of approximately $30\ \mu\text{m}$. Specifically, the flat depth in Figure 7 is the difference between the average nominal diameter, resulting from five measurements, and the average flat-to-sphere distance, also from five measurements (see Figure 5C). The five nominal diameter measurements had an average standard deviation of $0.44\ \mu\text{m}$, while the flat-to-sphere measurements had an average standard deviation of $0.92\ \mu\text{m}$. The greater standard deviation for the flat-to-sphere measurements is due in large part to the non-flatness of the flat (the “flat” is only nominally flat) combined with human operation of the micrometer.

TABLE 1: NUMBER OF BALLS IN OUTER LOOP OF TRUCK 2 INDUCED WITH FLATS AT EACH STAGE OF DEGRADATION.

Stage	Damaged Balls	Stage	Damaged Balls
0	None	20	13, 28, 2, 16
1	2, 16, 9, 25	21	9, 25, 5, 12
2	5, 12, 21, 29	22	21, 29, 7, 14
3	7, 14, 19, 27	23	19, 27, 32, 10
4	32, 10, 30, 3	24	30, 3, 20, 11
5	20, 11, 26, 15	25	26, 15, 31, 22
6	31, 22, 8, 24	26	8, 24, 13, 28
7	13, 28, 2, 16	27	2, 16, 9, 25
8	9, 25, 5, 12	28	5, 12, 21, 29
9	21, 29, 7, 14	29	7, 14, 19, 27
10	19, 27, 32, 10	30	32, 10, 30, 3
11	30, 3, 20, 11	31	20, 11, 26, 15
12	26, 15, 31, 22	32	31, 22, 8, 24
13	8, 24, 13, 28	33	13, 28, 2, 16
14	2, 16, 9, 25	34	9, 25, 5, 12
15	5, 12, 21, 29	35	21, 29, 7, 14
16	7, 14, 19, 27	36	19, 27, 32, 10
17	32, 10, 30, 3	37	30, 3, 20, 11
18	20, 11, 26, 15	38	26, 15, 31, 22
19	31, 22, 8, 24	39	8, 24, 13, 28

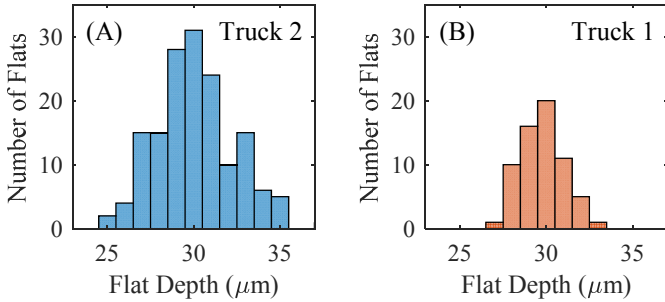


FIGURE 7: HISTOGRAM OF FLAT DEPTH FOR (A) TRUCK 2 AND (B) TRUCK 1.

The nominal flat depth of $30 \mu\text{m}$ was chosen to be large enough to influence the geometric error motions of the linear axis, without being too large as to be unrealistic of possible damage within a machine tool linear axis. The volume, v , of material removed by a flat is defined as

$$v = \frac{\pi}{3} d^2 (3r - d) \quad (1)$$

and the curved area, a , of the ball marred with the flat is

$$a = 2\pi r d \quad (2)$$

where d is the flat depth and r is the nominal ball radius. The metal balls were made of chromium steel with a nominal diameter of 3.965 mm . For a nominal flat depth, d , of $30 \mu\text{m}$ (see Figure 7), Eq. (1) shows that the nominal volume of metal material removed by a flat is about 0.0056 mm^3 , which is a relatively small volume. Also, Eq. (2) shows that the nominal area of metal marred by the flat is about 0.37 mm^2 , which is a

relatively small area. However, after 220 flats have been induced, the cumulative material removal is approximately 1.23 mm^3 and the cumulative marred area is about 0.82 cm^2 . These flats interact with the rails to influence the geometric error motions.

Theoretically, the surface roughness of the truck balls (not material volume) and the total damaged surface area are metrics that correlate with the geometric error motions, specifically the straightness and angular error motions. The average surface roughness, R_a , across all 208 metal balls in the trucks ($4 \text{ trucks} \times 2 \text{ loops per truck} \times 26 \text{ metal balls per loop}$) can be estimated via the material removal as

$$R_a \approx \bar{R}_a + \frac{V}{A_T} \quad (3)$$

where \bar{R}_a is the nominal average surface roughness [11] excluding the flats, V is the total cumulative volume of material removed by all flats at any moment, and A_T is the total cumulative surface area of all metal balls in the trucks (approximately equal to 103 cm^2). The balls were specified as Grade 25, which has a maximum allowable average surface roughness of $0.0508 \mu\text{m}$, so we assume that $\bar{R}_a = 0.0508 \mu\text{m}$. Consequently, after 220 flats have been induced for a total material removal of 1.23 mm^3 , Eq. (3) reveals that the average surface roughness across all metal truck balls is then approximately $0.17 \mu\text{m}$. Similarly, the relative damaged surface area, A_{rel} , is defined as

$$A_{\text{rel}} = \frac{A}{A_T} \quad (4)$$

where A is the total cumulative damaged ball area due to all flats at any moment. After 220 flats have been induced, Eq. (4) reveals that approximately 0.80% of the metal ball surface area has been damaged by the numerous flats. Thus, the 220 flats damage almost 1% of the total surface area, in addition to tripling the average surface roughness, of the metal balls.

This experiment and subsequent analysis explores the ability for such a significant change in surface roughness to be detected by an IMU-based methodology, based on changes detected in the geometric error motions of the linear axis. Figure 8 shows the surface roughness and relative damaged surface area calculated according to Eq. (3) and Eq. (4), respectively, for all stages of degradation. Because the depth of each flat is nominally $30 \mu\text{m}$ (Figure 7), the surface roughness and relative damaged surface area change relatively linearly with degradation stage.

Note that the nylon balls are not included in the surface roughness equation, Eq. (3), because the nylon balls bear insignificant loads. The nylon balls had a nominal diameter of 3.969 mm , which is $4 \mu\text{m}$ greater than the nominal diameter of 3.965 mm for the chromium steel balls. Therefore, the nylon balls will bear some nominal load. However, because nylon has such a relatively low modulus of elasticity compared to that for chromium steel, the nylon balls deflect easily under very low

loads. For example, the relatively small force due to the ratchet of the micrometer deflected the nylon balls about 72 μm . The low stiffness of the nylon balls means that the nylon balls act as metal-ball spacers without otherwise significantly influencing the geometric error motions.

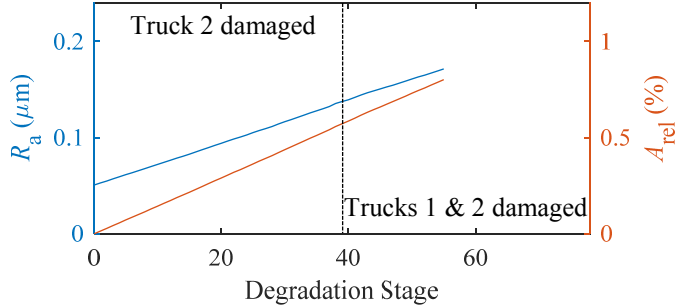


FIGURE 8: AVERAGE SURFACE ROUGHNESS AND RELATIVE DAMAGED SURFACE AREA OF ALL METAL BALLS WITHIN TRUCKS VERSUS DEGRADATION STAGE.

4. FEATURES FOR DATA ANALYSIS

The IMU and laser-based reference data that were gathered at each stage of degradation (Stage 0 to Stage 55) can now be used for analysis. The fifty (50) runs of time-sampled IMU data were processed to yield the error motions as functions of travel position (X values) [8, 9], while the ten (10) runs of laser-based reference data were already functions of position, being collected at nominal positions with an interval of 1 mm. Based on the rate gyroscope and accelerometer bandwidths and axis speed, the available spatial frequency range is between 0 and 2 cycles/mm (2000 m^{-1}). Hence, for each of the stages of degradation, there are fifty (50) IMU-based data runs and ten (10) reference-based data runs available for analysis.

The statistical time-domain features used in the analysis of this experiment are described in detail in Ref. [12]: peak value (PV), root-mean-square (RMS), standard deviation (σ), skewness (γ_1), kurtosis (γ_2), crest factor (CF), shape factor (SF), impulse factor (IF), and clearance factor (CLF). The feature formulas are given in Table 2, where \bar{y} denotes the average of a signal (y) and N denotes the number of data points in the signal. For the current implementation, each ‘signal’ is a geometric error motion as a function of position, or some transformation of the error motion, e.g., via filtering. The features were calculated for every instance of error motion data generated at each stage of degradation.

The features in Table 2 were applied to mean-subtracted, band-pass filtered signals. First, the error motions were bandpass filtered between spatial frequencies of 200 m^{-1} and 10⁴ m^{-1} , which have cutoff wavelengths of 5 mm and 0.1 mm, respectively. The cutoff wavelength of 0.1 mm is the smallest wavelength achievable, corresponding to the bandwidth of the rate gyroscopes (200 Hz) and the axis speed used for that frequency range (0.02 m/s). On the other hand, the cutoff wavelength of 5 mm is sufficient to capture any impacts from bearing faults, since bearing fault signatures are assumed to occur with wavelengths on the order of about 0.7 mm (the

nominal diameter of the flats) and less than about 12.4 mm (circumference of a single ball). Filtering was performed with a first-order, zero-phase digital Butterworth filter [13]. Second, to eliminate any portion of data that relates to the shape of the rail raceways, the mean of the filtered signals was removed. This means that for the fifty (50) runs of IMU-based data for each of the six degrees of freedom, the means of all 50 filtered signals were subtracted from each individual signal for feature analysis. Similarly, the filtering and mean-removal processes were applied to the ten (10) laser-based reference data for each stage of degradation.

TABLE 2: STATISTICAL FEATURES.

Feature Name	Formula
Peak Value	$PV(y) = \frac{1}{2}(\max(y) - \min(y))$
Root-Mean-Square	$RMS(y) = \sqrt{\frac{1}{N} \sum_{i=1}^N y_i^2}$
Standard Deviation	$\sigma(y) = \sqrt{\frac{1}{N-1} \sum_{i=1}^N (y_i - \bar{y})^2}$
Skewness	$\gamma_1(y) = \frac{\frac{1}{N} \sum_{i=1}^N (y_i - \bar{y})^3}{\sigma^3}$
Kurtosis	$\gamma_2(y) = \frac{\frac{1}{N} \sum_{i=1}^N (y_i - \bar{y})^4}{\sigma^4}$
Crest Factor	$CF(y) = \frac{PV(y)}{rms(y)}$
Shape Factor	$SF(y) = \frac{rms(y)}{\frac{1}{N} \sum_{i=1}^N y_i }$
Impulse Factor	$IF(y) = \frac{PV(y)}{\frac{1}{N} \sum_{i=1}^N y_i }$
Clearance Factor	$CLF(y) = \frac{PV(y)}{\left(\frac{1}{N} \sum_{i=1}^N \sqrt{ y_i }\right)^2}$

5. DATA ANALYSIS AND RESULTS

An example of a feature applied to the IMU-based data is Figure 9, which shows the standard deviation of each filtered error motion. There are 55 degradation stages, and there are fifty (50) runs at each stage, leading to fifty values of standard deviation at each stage. Specifically, the standard deviation in Figure 9 is the standard deviation of a bandpass filtered version of an error motion (see Section 4), denoted by a tilde over each error motion, e.g., \tilde{E}_{XX} and \tilde{E}_{AX} . At each stage, the blue box represents the middle 50 percent of the 50 values, and the black whiskers extend to the largest value that falls below $q_3 + 1.5(q_3 - q_2)$, or the smallest value that falls above $q_2 - 1.5(q_3 - q_2)$, where q_2 and q_3 are the 25th and 75th percentile respectively. Values that fall outside this range are classified as outliers, which are plotted as blue crosses in Figure 9. Also, the red line within each blue box is the median value for all 50 runs for that degradation stage.

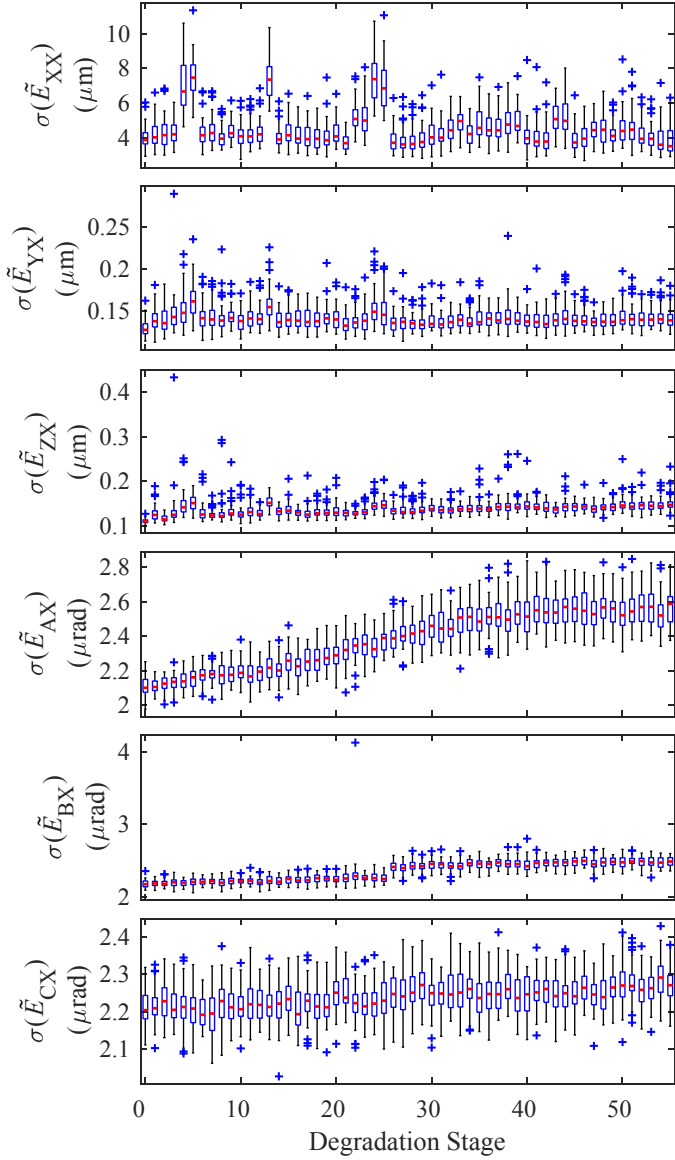


FIGURE 9: BOXPLOTS OF STANDARD DEVIATION OF FILTERED ERROR MOTION VERSUS DEGRADATION STAGE.

Some trends of the metric, $\sigma(\tilde{E}_{AX})$, with degradation stage are evident in Figure 9, while others are more unclear. For example, one clear trend is that $\sigma(\tilde{E}_{AX})$ increases fairly linearly from a value of about $2.1 \mu\text{rad}$ at Stage 0 to about $2.5 \mu\text{rad}$ at Stage 40, which is a $0.4 \mu\text{rad}$ increase in the metric. Then, the metric essentially stays constant after Stage 40. This difference in trends (linear versus constant metric) is related to which balls were damaged at each stage: metal balls of Truck 2 were only damaged until Stage 40, at which point new flats were induced only on the metal balls of Truck 1. Therefore, the difference in trends is due to the dependence of $\sigma(\tilde{E}_{AX})$ on the balls of the trucks, accounting for the linear trend before Stage 40 (due to damage within Truck 2) and the constant trend after Stage 40

(due to damage within Truck 1). Perhaps the physical mechanism that leads to the trend difference is the preload on each truck, with the preload being much greater on the balls of Truck 2 compared to Truck 1. A greater preload within Truck 2 could lead to a greater dependence of E_{AX} on changes to the balls within Truck 2.

One way to assess trends is to monitor a characteristic of a statistical population of the feature with degradation stage. Each of the boxplots in Figure 9 represents a statistical population at a given stage of degradation. As such, the statistical characteristics (mean, median, etc.) of each population can be monitored from stage to stage. Because median trends are visible in Figure 9, and the data has relatively large (but few) outliers, the median value is chosen instead of the mean for monitoring purposes. For the standard deviation feature, we can approximate the contribution of degradation to the median value. Based on the assumption that the additional signal (from degradation) and baseline signal (without degradation) are uncorrelated, this relationship can be represented as

$$\sigma_i^2 = \sigma_0^2 + \sigma_{d,i}^2 \quad (5)$$

where σ_0 is the standard deviation without degradation, and $\sigma_{d,i}$ is the contribution from degradation at the i^{th} stage of degradation. To ensure that the contribution from degradation is positive and begins at zero at Stage 0, the median contribution is approximated as

$$\hat{\sigma}_{d,i} = \sqrt{\hat{\sigma}_i^2 - \min(\hat{\sigma}_i)^2} - \hat{\sigma}_0 \quad (6)$$

where a ‘‘hat’’ denotes the median value, and the minimum function is for all median values. Equation (6) can be applied to the IMU-based data as well as the laser-based reference data.

Figure 10 shows the approximate contribution of degradation to the median standard deviation, $\hat{\sigma}_{d,i}$, for the IMU- and reference-based data for one DOF (roll angle). Even though the reference data has a lower noise than the IMU data (Figure 10A), the trend of the approximate contribution from degradation is very similar and within $0.5 \mu\text{rad}$ (Figure 10B). There appears to be a scaling difference between the IMU- and reference-based results for $\hat{\sigma}_d(\tilde{E}_{AX})$, which could be due to the differences in data collection (carriage dynamics, sensor bandwidths, thermal states, etc.). For the other five DOF, the differences are much larger than a scaling factor. Figure 11 compares the IMU- and reference-based approximate contribution of degradation for all six DOF. The medians trend at significantly different rates (for \tilde{E}_{YX} and \tilde{E}_{BX}) or even trend in opposite directions (for \tilde{E}_{ZX} and \tilde{E}_{CX}). A question then arises: How do we assess trends of features with degradation stage?

One way to assess the trends of features is to evaluate the correlations with degradation stage. The Pearson correlation coefficient, ρ_P , measures the linearity of a trend, while the Spearman correlation coefficient, ρ_S , measures the monotonicity of a trend [14]. Because both correlation coefficients have merit,

the geometric mean of their magnitudes, $\sqrt{|\rho_p||\rho_s|}$, can be used to quantitatively assess a trend. The closer the geometric mean is to the maximum possible value of one, the greater the correlation of a trend with degradation stage.

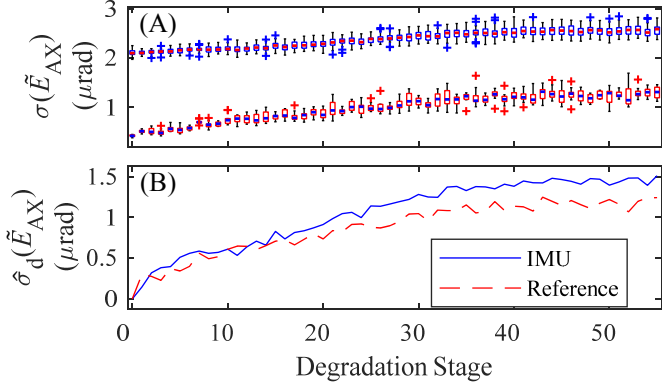


FIGURE 10: (A) BOXPLOTS OF STANDARD DEVIATION OF FILTERED ERROR MOTION BASED ON IMU DATA (BLUE BOXES AND CROSSES) AND REFERENCE DATA (RED BOXES AND CROSSES), AND (B) RELATIVE MEDIAN VALUES.

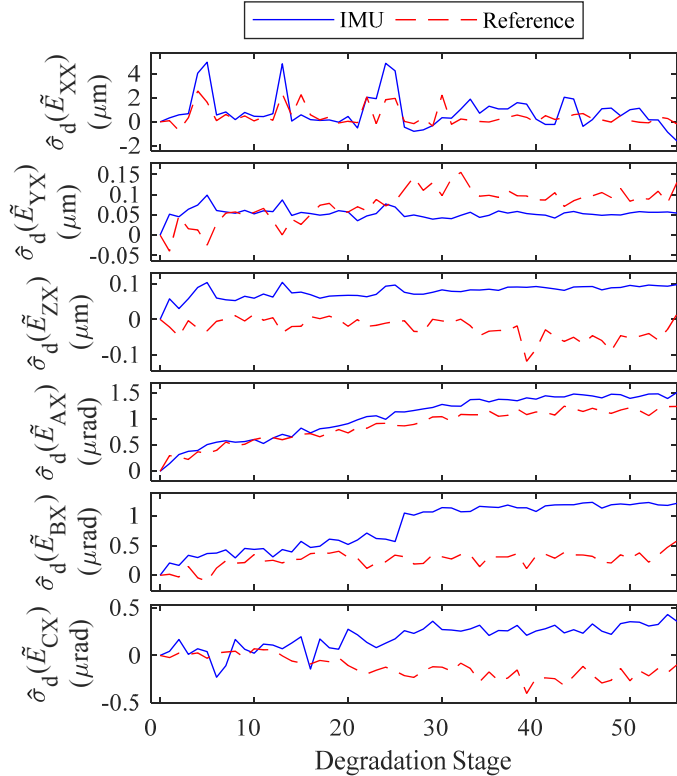


FIGURE 11: (A) RELATIVE MEDIAN VALUES FOR IMU- AND REFERENCE-BASED RESULTS.

The metric, $\sqrt{|\rho_p||\rho_s|}$, can be calculated for any statistical characteristic of any feature. Figure 12 shows the geometric mean of the Pearson and Spearman coefficients for the median of each of the nine statistical features (Table 2). Each of the six

degrees of freedom has a different value of $\sqrt{|\rho_p||\rho_s|}$ for each of the nine features. Visual inspection shows that there can be significant variety among the metric values for the degrees of freedom, leading to a “skyscraper” effect in Figure 12. Nonetheless, some features trend with the degradation of the outer loop balls, since many of the geometric means in Figure 12 have magnitudes above 0.5.

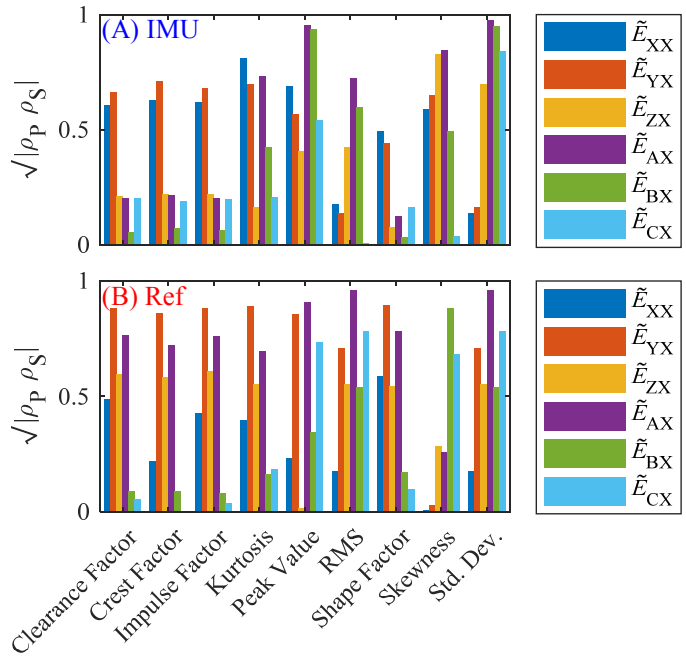


FIGURE 12: GEOMETRIC MEAN OF PEARSON AND SPEARMAN CORRELATION COEFFICIENTS FOR MEDIAN OF EACH STATISTICAL FEATURE BASED ON DATA FROM (A) IMU AND (B) REFERENCE.

In order to quantitatively assess the metrics in the aggregate for a feature, the arithmetic mean, $\bar{\rho}$, is defined as

$$\bar{\rho} = \text{mean}(\sqrt{|\rho_p||\rho_s|}) \text{ for six values for each feature} \quad (7)$$

Figure 13 compares the arithmetic mean of the IMU- band reference-based medians for the nine statistical features (Table 2). The IMU-based values of $\bar{\rho}$ range from about 0.3 (shape factor feature) to about 0.7 (peak value and standard deviation feature), while reference-based values of $\bar{\rho}$ range from about 0.5 (skewness feature) to about 0.7 (RMS and standard deviation features). Therefore, the standard deviation feature has, on average, the largest value of $\bar{\rho}$ and is therefore chosen as the feature to be investigated for monitoring purposes.

Not only can the median value of standard deviations be used for monitoring trends (Figure 11) in a physical sense of micrometers or microradians, but the Wilcoxon rank sum test can be used to determine whenever the median value of one population (for Stage 1 and beyond) has deviated significantly from that for the initial population (for Stage 0) [14]. If the Wilcoxon rank sum test probability, P , is below 0.05 (5%), the

distribution for that stage is statistically different from the initial stage. In that case, the hypothesis, H , equals 1, because the hypothesis of a statistically significant change due to degradation is true. On the other hand, whenever the probability, P , is not below 0.05 (5%), the hypothesis is false ($H = 0$), since the median value of the given distribution has not changed much from the initial value for Stage 0; degradation is unclear.

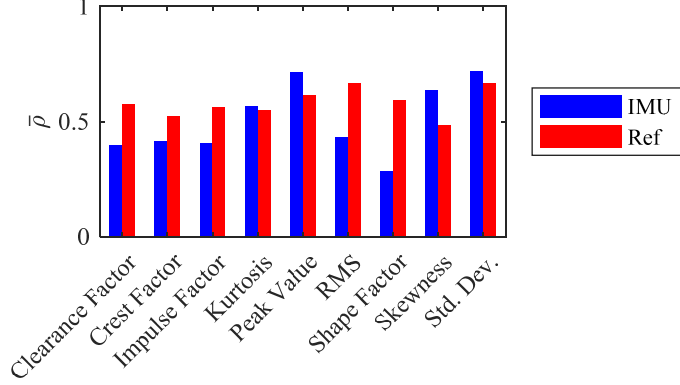


FIGURE 13: ARITHMETIC MEAN OF GEOMETRIC MEANS FOR MEDIAN OF EACH STATISTICAL FEATURE OF IMU-BASED AND REFERENCE-BASED RESULTS.

Figure 14 shows the probability, P , and hypothesis, H , values for $\sigma(\tilde{E}_{YX})$. The IMU detects a change at Stage 1, which is much earlier than when the reference detects a change at Stage 16, despite the reference yielding a much greater correlation ($\sqrt{|\rho_P||\rho_S|} = 0.7$) than the IMU ($\sqrt{|\rho_P||\rho_S|} = 0.2$) for standard deviation of \tilde{E}_{YX} in Figure 12. To smooth abrupt changes of P for condition monitoring purposes, filtered versions of P and H , denoted as P_F and H_F , are also shown in Figure 14. The P curve is filtered with a first-order Savitzky-Golay filter of length 11 to yield P_F , which then results in H_F via the 5% threshold. In Figure 14A, the H_F value switches at Stage 6 because the Savitzky-Golay filter of length 11 ($= 5 + 1 + 5$) smooths out the abrupt shift of P at Stage 1 to last until Stage 6 ($= 1 + 5$).

Figure 15 shows the P_F curves for standard deviation for all degrees of freedom. The IMU-based results cross the 5% threshold only once, while the reference-based results sometimes cross back and forth across the 5% threshold, despite increasing degradation. Furthermore, the IMU-based results cross the 5% threshold at earlier stages than the reference-based results, showing how the IMU is perhaps more sensitive and better suited for monitoring purposes. The only degree of freedom that does not cross the 5% threshold is \tilde{E}_{XX} , because the positioning error motion is not significantly affected by truck ball degradation.

Figure 15 can be combined with Figure 11 to determine the minimum significant changes of standard deviation for five DOF (positioning error excluded). The IMU-based values in Figure 11 at the threshold crossings in Figure 15 are either about $0.05 \mu\text{m}$ (for translational error motions) or $0.5 \mu\text{rad}$ (for angular error motions). Therefore, $0.05 \mu\text{m}$ and $0.5 \mu\text{rad}$ are the minimum statistically-significant changes of standard deviation due to

degradation for the IMU-based results. In fact, these two minima are essentially the same, because the characteristic distance between trucks is roughly 0.1 m, which means that a change of $0.05 \mu\text{m}$ would create an angular change of about $0.5 \mu\text{rad}$ ($= 0.05 \mu\text{m}/0.1 \text{m}$). Finally, the crossing locations in Figure 15A range from Stage 6 to Stage 28, which relate to 0.09% or 0.4% of damage to the total metal ball surface area. Consequently, as little as 0.09% of total metal ball area damage can yield a statistically significant change of standard deviation.

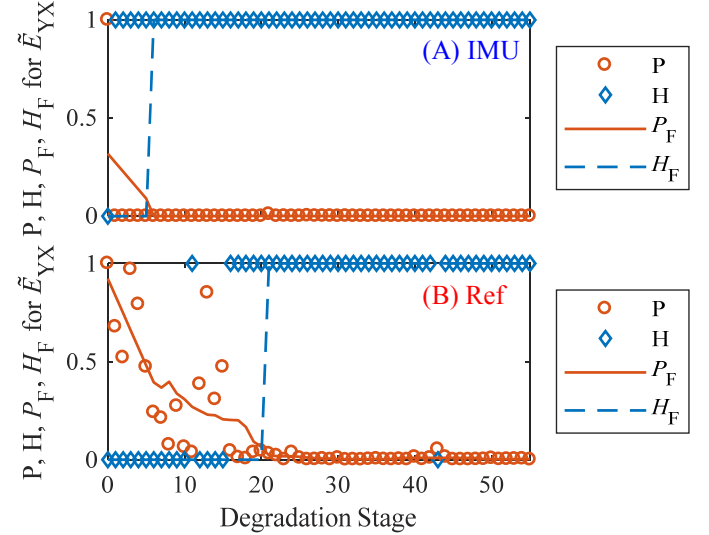


FIGURE 14: WILCOXON RANK SUM TEST, AND ITS FILTERED FORM, FOR $\sigma(\tilde{E}_{YX})$ BASED ON DATA FROM (A) IMU AND (B) REFERENCE.

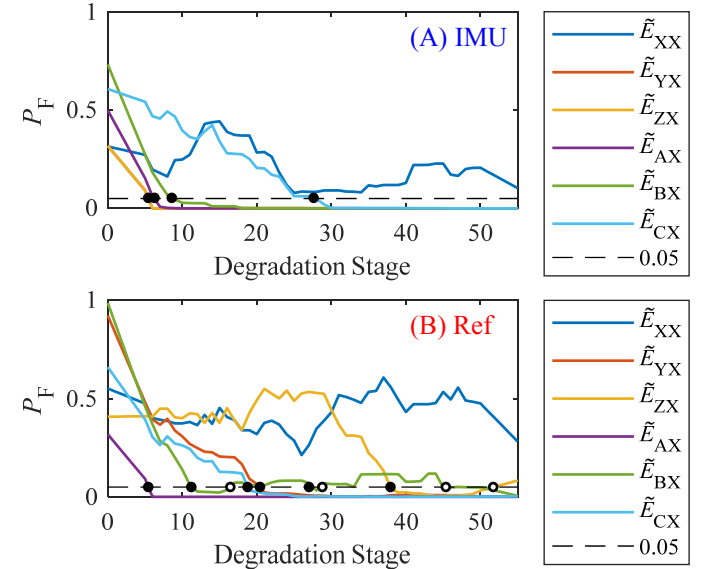


FIGURE 15: FILTERED VERSION OF WILCOXON RANK SUM TEST VERSUS DEGRADATION STAGE, BASED ON DATA FROM (A) IMU AND (B) REFERENCE. DOWNWARD/UPWARD CROSSINGS WITH THE (DASHED) FIVE PERCENT LINE ARE DENOTED WITH BLACK/WHITE FILLED CIRCLES.

6. CONCLUSIONS

An inertial measurement unit was studied for its ability to measure changes in geometric error motions due to induced faults on the recirculating ball bearings of two carriage trucks within a linear axis. Each truck was modified with an access hole that allowed the metal balls in the outer loop of the truck to be progressively removed and degraded. In this experiment, each of the metal balls in the outer loop of two trucks were damaged in a specific order until each ball had six flats, each with a nominal depth of 30 μm . For each stage of degradation, four new flats were induced and then fifty (50) runs of IMU data were collected in addition to ten (10) runs of laser-based reference data. After 220 flats had been induced, approximately 0.80% of the metal ball surface area was damaged by the numerous flats, and the average surface roughness was changed by about 0.11 μm .

For each stage of degradation, the fifty runs of IMU data and ten runs of reference data were analyzed with the nine features (standard deviation, kurtosis, etc.) used for rotating machinery systems. Trends in the median value of the statistical populations were determined via the Pearson and Spearman correlation coefficients. The standard deviation feature had one of the greatest correlations with degradation among both the IMU and reference data, so the standard deviation feature was used for the rest of the analysis. Subsequently, the Wilcoxon rank sum test was used to reveal an ability of the standard deviation feature to detect statistically significant changes as small as 0.05 μm or 0.5 μrad , corresponding to a total damaged surface area of truck balls of less than 0.1 percent.

Therefore, results showed that the IMU-based monitoring system has promise for online, data-rich, integrated diagnostics and prognostics of linear axes system health. Feature changes due to increasing degradation were identified in the median of standard deviation and other features. Pearson and Spearman correlation analysis provided a high-level view of these trends and insight into how to select a feature for monitoring. On the other hand, the Wilcoxon rank sum test provided a low-level view of how to determine statistical lower bounds, for thresholding purposes, within future online monitoring systems.

Future work includes analysis of filtered components with spatial frequencies that are different than those used in this study, as well as the incorporation of the inductive proximity sensor data. The “smart truck” concept, used to detect the phase of the outer loop of balls, could be used to study the influence of the balls and their damage on the geometric error motions.

ACKNOWLEDGEMENTS

The authors thank Casey Shatzley and the Fabrication Technology Office (National Institute of Standards and Technology) for modifying the trucks used in the experiments.

NIST DISCLAIMER

Certain commercial equipment, instruments, or materials are identified in this paper in order to specify the experimental procedure adequately. Such identification is not intended to imply recommendation or endorsement by the National Institute of Standards and Technology, nor is it intended to imply that the

materials or equipment identified are necessarily the best available for the purpose. This material is declared a work of the U.S. Government and is not subject to copyright protection in the United States. Approved for public release; distribution is unlimited.

REFERENCES

- [1] Altintas Y, Verl A, Brecher C, Uriarte L, Pritschow G (2011) Machine Tool Feed Drives. *CIRP Annals-Manufacturing Technology* 60(2):779-796.
- [2] Li Y, Wang X, Lin J, Shi S (2014) A Wavelet Bicoherence-Based Quadratic Nonlinearity Feature for Translational Axis Condition Monitoring. *Sensors (Basel)* 14(2):2071-2088.
- [3] Zhou Y, Mei X, Zhang Y, Jiang G, Sun N (2009) Current-Based Feed Axis Condition Monitoring and Fault Diagnosis. 4th IEEE Conference on Industrial Electronics and Applications, ICIEA 2009, 1191-1195.
- [4] Uhlmann E, Geisert C, Hohwieler E (2008) Monitoring of Slowly Progressing Deterioration of Computer Numerical Control Machine Axes. *Proceedings of the Institution of Mechanical Engineers Part B-Journal of Engineering Manufacture* 222(10):1213-1219.
- [5] International Organization for Standardization (2012) ISO 230-1 - Test Code for Machine Tools – Part 1: Geometric Accuracy of Machines Operating under No-Load or Quasi-Static Conditions.
- [6] Khan AW, Chen W (2008) Calibration of CNC Milling Machine by Direct Method. 2008 International Conference on Optical Instruments and Technology: Optoelectronic Measurement Technology and Applications, 7160:716010.
- [7] Teti R, Jemielniak K, O'Donnell G, Dornfeld D (2010) Advanced Monitoring of Machining Operations. *CIRP Annals-Manufacturing Technology* 59(2):717-739.
- [8] Vogl GW, Donmez MA, Archenti A (2016) Diagnostics for Geometric Performance of Machine Tool Linear Axes. *CIRP Annals-Manufacturing Technology* 65(1):377-380.
- [9] Vogl GW, Donmez MA, Archenti A, Weiss BA (2016) Inertial Measurement Unit for On-Machine Diagnostics of Machine Tool Linear Axes. Annual Conference of the Prognostics and Health Management Society 2016, 7.
- [10] Vogl GW, Sharp ME (2017) Diagnostics of Machine Tool Linear Axes Via Separation of Geometric Error Sources. Annual Conference of the Prognostics and Health Management Society,
- [11] Black JT, Kohser RA (2012) *DeGarmo's Materials and Processes in Manufacturing*. 11th ed. John Wiley & Sons, Inc., USA.
- [12] Jameson J, Vogl GW (2018) Comparative Analysis of Bearing Health Monitoring Methods for Machine Tool Linear Axes. Society for Machinery Failure Prevention Technology 2018 (MFPT 2018), 1-16.
- [13] Oppenheim AV, Schafer RW, Buck JR (1999) *Discrete-Time Signal Processing*. 2nd ed. Prentice Hall, Upper Saddle River, NJ.
- [14] Gibbons JD, Chakraborti S (2003) *Nonparametric Statistical Inference*. 4th ed. Marcel Dekker Inc., New York.